Solar Phys (2012) 277:337–354
DOI 10.1007/s11207-011-9903-6

Filament Eruption in NOAA 11093 Leading to a Two-Ribbon M1.0 Class Flare and CME

P. Vemareddy · R.A. Maurya · A. Ambastha

Received: 17 March 2011 / Accepted: 11 November 2011 / Published online: 8 December 2011

Abstract We present a multi-wavelength analysis of an eruption event that occurred in active region NOAA 11093 on 7 August 2010, using data obtained from SDO, STEREO, RHESSI, and the GONG Hα network telescope. From these observations, we inferred that an upward slow rising motion of an inverse S-shaped filament lying along the polarity inversion line resulted in a CME subsequent to a two-ribbon flare. Interaction of overlying field lines across the filament with the side-lobe field lines, associated EUV brightening, and flux emergence/cancelation around the filament were the observational signatures of the processes leading to its destabilization and the onset of eruption. Moreover, the time profile of the rising motion of the filament/flux rope corresponded well with flare characteristics, *viz.*, the reconnection rate and hard X-ray emission profiles. The flux rope was accelerated to the maximum velocity as a CME at the peak phase of the flare, followed by deceleration to an average velocity of 590 km s^{-1}. We suggest that the observed emergence/cancelation of magnetic fluxes near the filament caused it to rise, resulting in the tethers to cut and reconnection to take place beneath the filament; in agreement with the tether-cutting model. The corresponding increase/decrease in positive/negative photospheric fluxes found in the post-peak phase of the eruption provides unambiguous evidence of reconnection as a consequence of tether cutting.

Keywords Active regions, magnetic fields · Corona, active · Flares, dynamics

P. Vemareddy (✉) · R.A. Maurya · A. Ambastha
Udaipur Solar Observatory (Physical Research Laboratory), P.O. Box 198, Dewali, Badi Road, Udaipur 313 001, India
e-mail: vema@prl.res.in

R.A. Maurya
e-mail: ramajor@prl.res.in

A. Ambastha
e-mail: ambastha@prl.res.in

1. Introduction

Solar filament eruptions are energetic events occurring due to the explosive release of magnetic energy. Understanding the driver and trigger mechanisms of these eruptions is one of the most challenging, ongoing research topics in solar physics. These events manifest as prominence eruptions if seen at the limb, and as filament eruptions if seen against the disk. They can be broadly divided into two classes:

i) ejective eruptions which give CMEs and long duration two-ribbon flares, and
ii) confined eruptions which give short duration flares.

However, there are also filament/prominence eruptions that are not associated with any flares. What defines the eruption to be ejective or confined event remains an unanswered question. (For detailed reviews on the theories of eruptions, refer to Priest and Forbes (2002) and Lin, Soon, and Baliunas (2003).)

In filament eruptions, one commonly observed feature in chromospheric Hα images is two bright flare ribbons separating away as the flare progresses. This process is explained as follows: The reconnection of magnetic field lines is believed to be the underlying mechanism for energy release as proposed by Carmichael (1964), Sturrock (1966), Hirayama (1974) and Kopp and Pneuman (1976). As a coronal magnetic flux rope loses equilibrium and travels upwards, an extended reconnection current sheet (RCS) is formed underneath. The magnetic reconnection in this RCS releases most of the magnetic energy stored in the magnetic field configuration (Forbes and Priest, 1984; Lin and Forbes, 2000). Charged particles can be effectively accelerated by the electric field in the RCS (Martens and Young, 1990; Litvinenko and Somov, 1995). Some particles, energized during a solar flare, gyrate around the field lines and propagate toward the underlying foot points, precipitating at different layers of the solar atmosphere to produce a two-ribbon flare. The separating motion of these chromospheric flare ribbons is believed to provide a signature of the reconnection process occurring progressively higher up in the corona. This is the standard flare model scenario. All eruption models lead to this standard model in the onset phase of eruption.

Several ideas have been advanced for explaining the onset mechanism of the eruption (Klimchuk, 2001; Forbes, 2006; Moore and Sterling, 2006). In the tether-cutting model proposed by Moore and LaBonte (1980) and further elaborated by Moore *et al.* (2001), the magnetic tension restraining the sheared core field of a bipolar magnetic arcade is released by internal reconnection above the polarity inversion line (PIL). Evidence for the tether-cutting model can be found in several recent observational studies (Liu *et al.*, 2007; Wang, 2006; Yurchyshyn *et al.*, 2006). External tether-cutting or "breakout" reconnection is similar to tether cutting in that it is a tension–release mechanism via reconnection. But here it occurs between the arcade envelope of the erupting field and an overarching restraining, reversed field of quadrupolar magnetic configuration (Antiochos, 1998; Antiochos, DeVore, and Klimchuk, 1999). Flux cancelation (Martin, Livi, and Wang, 1985; Martin, 1989), emergence of twisted flux ropes from below the surface (Leka *et al.*, 1996), and ideal MHD instability (Kliem and Török, 2006; Fan and Gibson, 2007) are some other mechanisms proposed to explain the eruption process.

Although there exist several proposed mechanisms, it is difficult to disentangle as to which particular mechanism is responsible for the fast eruption in complex active regions (ARs). This difficulty arises due to a wide variety of dynamic processes involved in such ARs. Therefore, we have selected a filament eruption event that occurred in a relatively simple AR, NOAA 11093 on 7 August 2010, which led to an M1.0 class two-ribbon flare and a fast CME. Our aim in this study is to understand the driver and trigger mechanisms of the

eruption and associated processes. We investigate various possible conditions of the eruption process in relation to flux emergence/cancelation at selected locations. From a morphological analysis, we attempt to find the triggering mechanism of the flare. We will derive the flare energetics in order to quantify the characteristics of this flare, and then compare it with previous such studies.

The advantage of high cadence and high resolution multi-wavelength observations has already been stressed by earlier studies (Liu *et al.*, 2005, 2007; Wang and Sheeley, 1999). In the present study, we utilize the unique opportunity of coordinated observations in multi-wavelength channels corresponding to different atmospheric heights provided by Atmospheric Imaging Assembly (AIA; Lemen *et al.*, 2011) and Helioseismic and Magnetic Imager (HMI; Schou *et al.*, 2011) on board *Solar Dynamics Observatory* (SDO).

The rest of the paper is organized as follows: The observational data and reduction procedures are presented in Section 2. Results and discussion are described in Section 3, while Section 4 gives the summary and conclusions.

2. Observational Data and Reduction

The eruption event in AR NOAA 11093 (N12° E31°) occurred on 7 August 2010. It produced a GOES M1.0 class flare starting at 17:55 UT and peaking at 18:20 UT. This event was covered by SDO's AIA and HMI, *Reuven Ramaty High-Energy Solar Spectroscopic Imager* (RHESSI; Lin *et al.*, 2002), as well as by the ground-based GONG Hα network telescope at Big Bear Solar Observatory (BBSO). The associated CME was detected by the COR1 coronagraph (Thompson *et al.*, 2003) on board both the Ahead and Behind satellites of *Solar TErrestrial RElations Observatory* (STEREO) which were separated by about 150°.

AIA takes multi-wavelength images at a pixel size of 0″.6 and 12 s cadence. To study the flaring plasma, we focused on the images obtained in 94 Å (Fe XVIII; $\log T = 6.8$), together with 171 Å (Fe IX; $\log T = 5.8$) corresponding to the upper transition region, and 304 Å (He II; $\log T = 4.8$) corresponding to the chromosphere and lower transition region. Images were added to enhance the signal to noise ratio, giving a cadence of 1 min. We have used the preprocessed images (level 1.0) provided after calibration, involving bad pixel correction, aligning, and scaling.

HMI makes measurements of the line-of-sight (LOS) magnetic field of the full solar disk at 6173 Å with a pixel size of 0″.5 and 45 s cadence with a sensitivity of 10 gauss (G). We have rotated the level-1.0 images so that the solar north is up. The scaling of data was done using the header information. We have summed every four images in order to increase the signal to noise ratio, giving a cadence of 3 minutes.

COR1 is an internally occulted coronagraph and is one of the STEREO SECCHI suite of remote sensing telescopes. It takes observations of CMEs from 1.3 to 4 solar radii in three different polarization angles every five min. We have used `secchi_prep.pro` and `cor1_quickpol.pro` routines in the STEREO software package to process the images and finally to get total polarization brightness images. For observing ejected material within 1.2 $R_{\odot}$, we have also examined images taken with Extreme Ultraviolet Imager (EUVI) of SECCHI on board STEREO-A.

We obtained Hα 6563 Å filtergrams at a pixel size of 1″ and 1 minute cadence from the GONG telescope operating at BBSO.

All full disk images obtained from different instruments were aligned by differentially rotating to a reference image at 18:00 UT. The offset was corrected after remapping and by

overlaying magnetic contours on images taken with different instruments. We have used the standard Solar SoftWare (SSW) library routines for our study.

3. Results and Discussion

3.1. Filament Evolution Leading to the Two-Ribbon M1.0 Flare

3.1.1. Morphology

Figure 1 (left panel) shows an HMI magnetogram of AR NOAA 11093 taken on 7 August 2010 at 17:10 UT. The AR showed a simple magnetic configuration reported as β-class by NOAA/USAF AR summary issued on 7 August 2010. The GONG Hα filtergram of the AR with contours of the LOS magnetic field is shown in the right panel. It consisted of a single main sunspot and an inverse S-shaped filament with its one end connected to the sunspot, as observed more than 1 h before the eruption event ensued. These images show the polarity of the dominant main sunspot and the diffused fluxes of opposite polarities surrounding the filament.

The filament was oriented in nearly the NE–SW direction along the PIL. We have concentrated our study mainly on the time interval of 17:00 – 20:00 UT for identifying the changes occurring in the morphological structure as well as the connectivity of field lines in the AR leading to the filament eruption and the flare.

The light curves of the flare in different wavelengths are shown in Figure 2. The gray shaded region from the start to the peak time of GOES flux represents the impulsive phase of the flare. The decay phase of GOES soft X-ray flux lasted over 3 h from the peak time, implying that this relatively small M1.0 class flare was a long duration event (LDE). The AIA 304 Å and Hα profiles essentially followed the GOES profiles, peaking at around 18:20 UT. However, AIA 94 and 171 Å profiles did not agree well in the impulsive phase, and

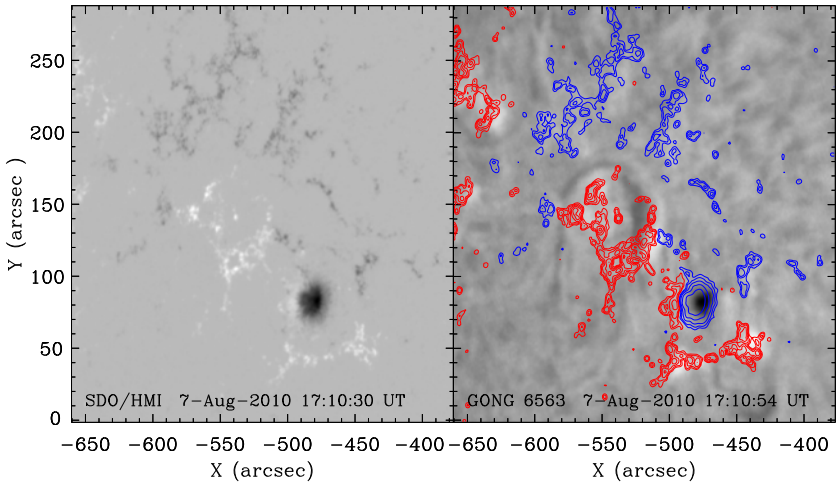

Figure 1 HMI line-of-sight magnetogram (left), and GONG Hα filtergram (right) of NOAA 11093 overlaid with red (blue) contours corresponding to positive (negative) magnetic polarities. North is directed upward in these and subsequent maps.

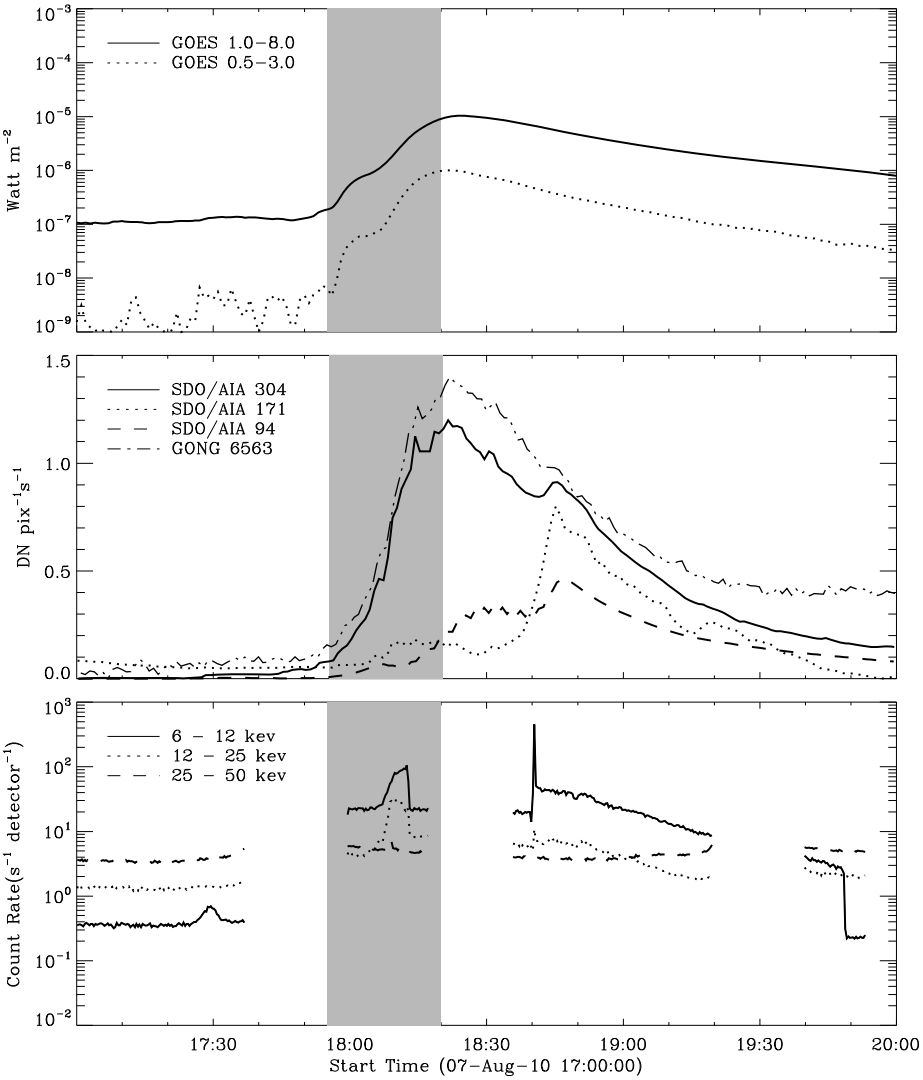

Figure 2 Light curves of the M1.0 class flare of 7 August 2010 in AR NOAA 11093: (top) GOES soft X-rays, (middle) AIA wavelengths and GONG Hα, and (bottom) RHESSI hard X-rays. The gray shaded region represents the impulsive phase of the flare as inferred from GOES soft X-rays. Gaps in RHESSI light curves are due to the spacecraft night and its passage through the South Atlantic Anomaly.

peaked much later at 18:45 UT. By examining the corresponding images, we found that the delayed peaking in these wavelengths corresponded with the post-flare loops that appeared in the decay phase.

The RHESSI hard X-ray (HXR) profiles show two gaps owing to the spacecraft night and its passage through the South Atlantic Anomaly. However, the available data in the shaded region, *i.e.*, the impulsive phase of the flare, clearly show a short duration enhancement in the level of HXR emissions in the 6 – 12 and 12 – 25 keV channels. Notably, however, no enhancement was seen in the harder emission in the 25 – 50 keV channel.

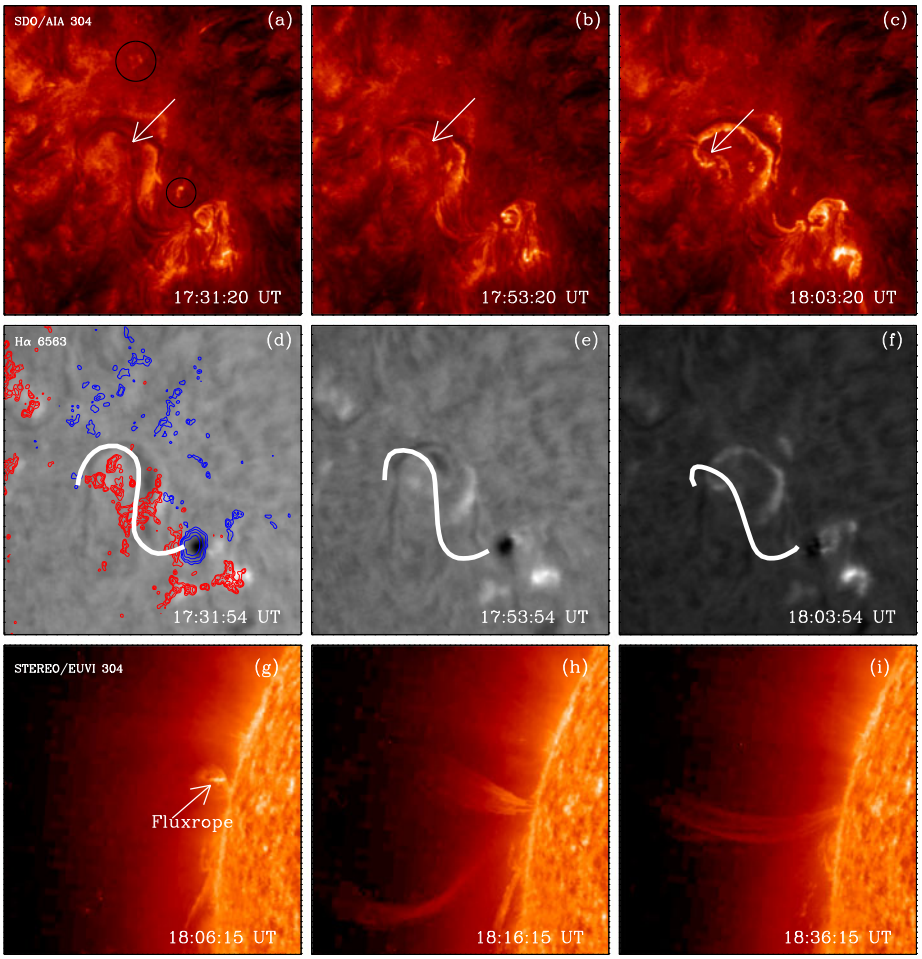

Figure 3 (Top row) Images of AIA 304 Å exhibiting a rising motion of the flux rope lying along PIL (marked by arrows) and the two brightening regions indicated by black circles. (Middle row) Hα images showing the corresponding morphological changes in the chromosphere. White thick curves drawn on these images represent the observed rising flux rope as seen in the 304 Å images at respective times. In panel (d), the overlaid red (blue) contours represent positive (negative) polarities. (Bottom row) The rising motion of the flux rope observed in STEREO-A/EUVI 304 Å at the east limb.

From movies made using the images in Hα and AIA channels, we observed that a flux rope having an average diameter of 6.9 Mm ($\approx 9''.5$) started to rise from the inner core of the filament at around 17:40 UT. Figure 3(a – c) shows, as pointed out by arrows, the rise of the flux rope connecting the sunspot and the other end of the filament elbow. The projection of this flux rope onto the chromosphere is seen as a dark shadow moving toward east and disappearing after 18:04 UT. At that time it had risen high, nearly vertical to the disk plane. About 15 min after the start of its rise, the flare brightenings appeared; first the northern ribbon and then the southern one. The rise of the filament was seen as a plasma jet ejection in the EUVI images of STEREO-A in 304 Å (Figure 3(g – i)). STEREO-A and B were separated by 150°, and STEREO-B was situated at 71° west from the Earth. AR 11093 was

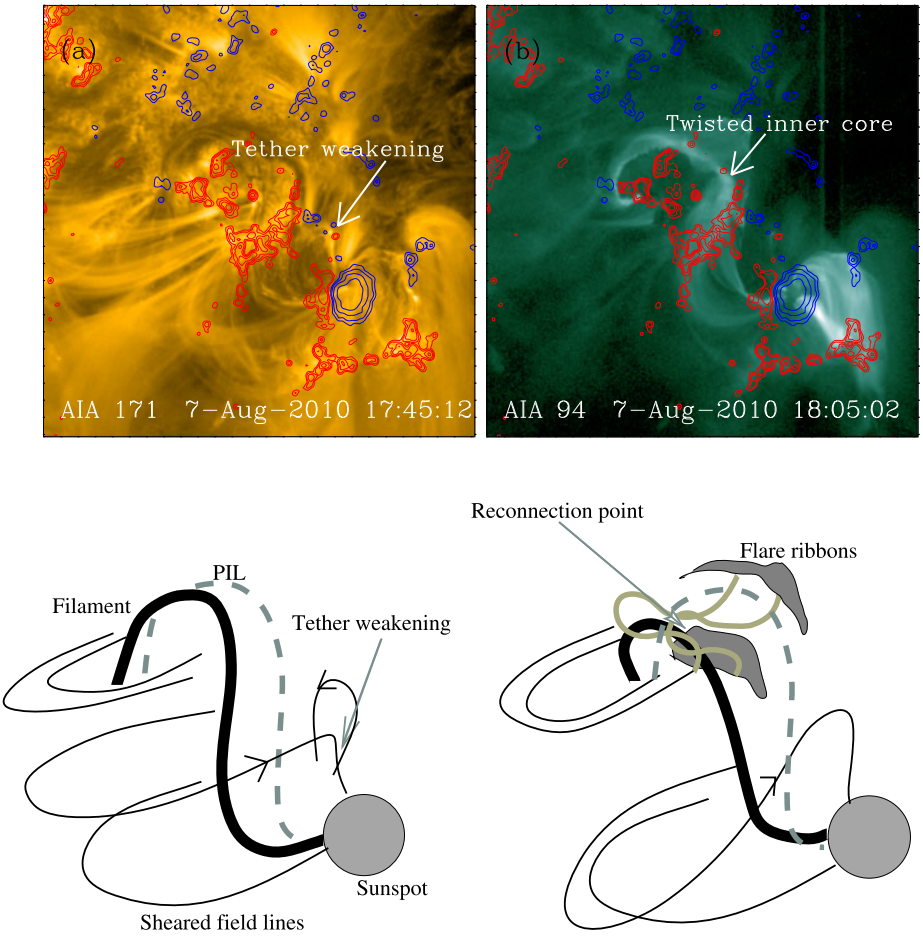

Figure 4 Top: Field-line topology before (a) and after (b) the onset of the eruption as seen in 171 and 94 Å channels, respectively, with superposed magnetic field contours. Bottom: Schematic drawings of how the rising motion of the flux rope/filament is triggered by tether weakening due to the interaction between the side-lobe field lines with the twisted overlying field lines from the sunspot. This rising motion enhanced the twist in the inner core of the filament further, forming a current sheet beneath it. The twisted inner-core loops can be clearly seen in panel (b).

36° west of STEREO-B central meridian and 24° away from the east limb of STEREO-A. Therefore, the flux rope was not visible till 18:03 UT with STEREO-A. Furthermore, from STEREO-B the event was not as clearly visible as in AIA 304 Å due to the lower spatial resolution ($\approx 1''.6$/pixel).

In Figure 4 we provide schematic drawings of this eruption event constructed by a careful examination of observed plasma tracers using a series of 171 and 94 Å images. The EUV brightening in the smaller of the two encircled regions in Figure 3(a) resulted due to the interaction between the overlying sheared field lines from the sunspot and the side-lobe field lines, as shown in Figure 4(a). This interaction substantially weakened the overlying field lines, allowing the flux rope to rise upward. This rising motion formed a current sheet in the cusp shaped region defined by field lines connecting the two polarities on either side

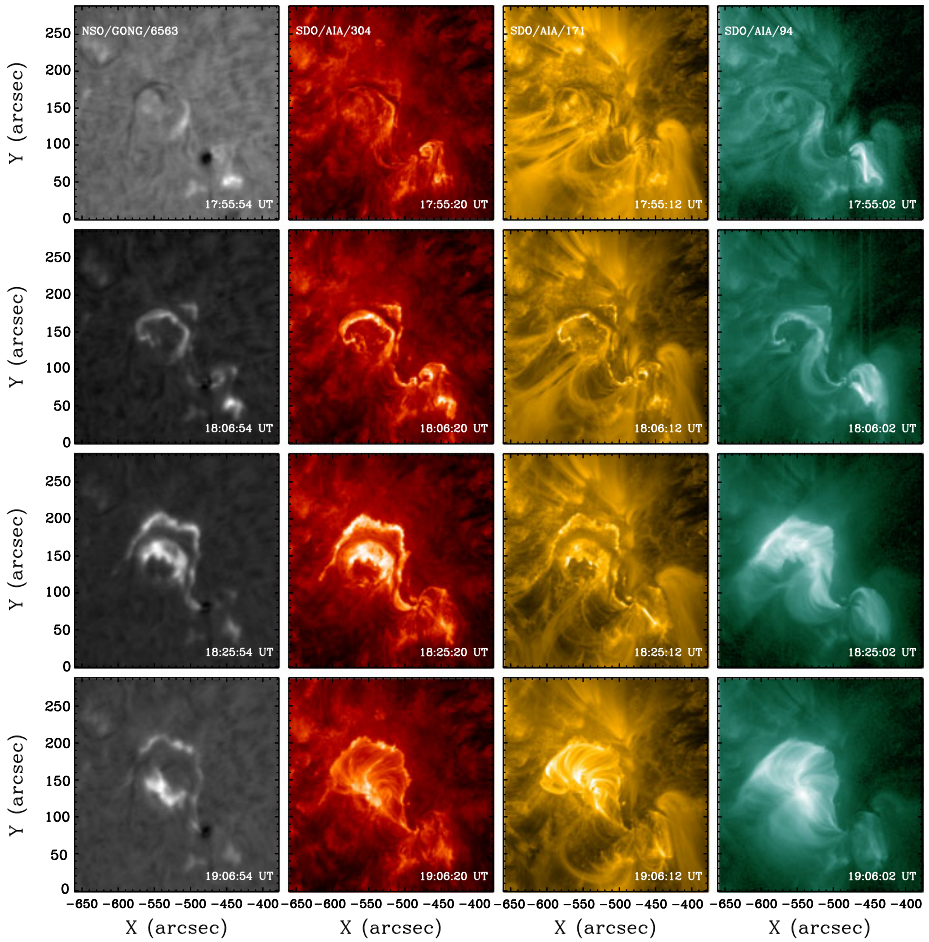

Figure 5 A collection of images showing the filament evolution during various phases of the flare – start (row 1), impulsive (rows 2 and 3), and decay (row 4) as observed in GONG Hα and AIA wavelengths corresponding to successively higher atmospheric layers.

of the filament, leading to the onset of an internal reconnection to commence the flare. In the 94 Å image (Figure 4(b)), the twisted bright flux system can be seen in the inner core below the flux rope. It is important to notice that the bright flux system appeared only in 94 Å because the soft X-ray emitting plasma was created due to the reconnection by the above process. This scenario agrees well with the model of Moore *et al.* (2001) that describes "tether cutting" as the trigger mechanism. It is worth mentioning that the tether weakening first occurred at the location of the brightening and then proceeded further in the core region beneath the filament. Tether cutting as a trigger for the onset of eruption within the erupting system was addressed by Yurchyshyn *et al.* (2006) in a quadrupolar configuration. We will discuss the magnetic flux changes at the locations of these brightenings in Section 3.3.

Figure 5 is a collection of multi-wavelength images illustrating the filament eruption and the flare in Hα and various AIA channels corresponding to successively higher atmospheric layers (from left to right columns). Rows correspond to the time of start (top), impulsive

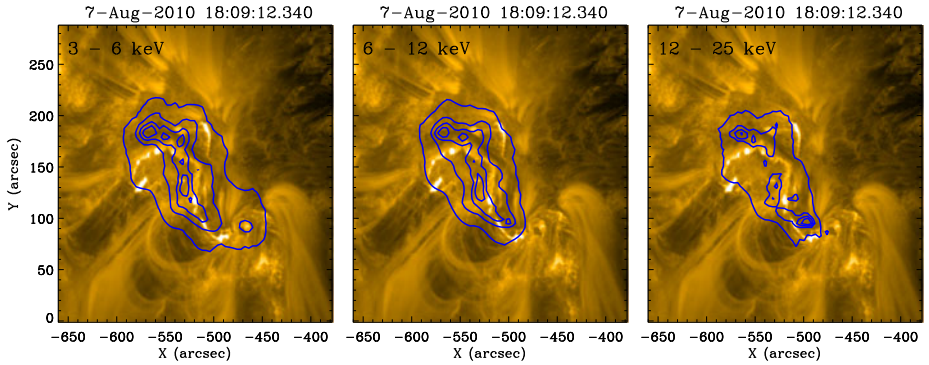

Figure 6 Contours of RHESSI HXR intensities overlaid on the AIA 171 Å image at 18:09 UT in three energy bands: 3 – 6 keV (left), 6 – 12 keV (middle), and 12 – 25 keV (right), reconstructed by the CLEAN algorithm with one minute integration time. Contour levels correspond to 50, 70, 80 and 90% of respective peak flux.

(second and third), and decay (bottom) phases of the flare. The first column shows the flare ribbons in the chromospheric Hα line. As time progressed, the flare ribbons brightened and separated away up to the peak time 18:25 UT, and decayed thereafter. Images in the second column correspond to the AIA 304 Å channel, showing the flare ribbons in the upper chromosphere, along with the overlying field lines filled with 6×10^4 K plasma. Post-flare loops connecting the flare ribbons are clearly seen in the decay phase. These post-flare loops gave rise to the second peak of the 304 Å light curve in Figure 2 (middle). In the third column, AIA 171 Å images show plasma loops more clearly as these are sensitive to $T \approx 6 \times 10^5$ K. The fourth column corresponds to AIA 94 Å images showing plasma loops at even higher temperatures ($\approx 6 \times 10^6$ K). We can observe here an increased twist in the core flux system due to the tether-cutting reconnection with an increased flux rope height (18:06:02 UT frame). It is important to note that this twisted flux system was not visible in 304 and 171 Å wavelengths corresponding to lower heights. Once the main reconnection phase commenced, these twisted flux system below the flux rope, as seen at 18:06:02 UT in the inner core of the filament, relaxed to arcades of lower twist seen at 19:06:26 UT in the decay phase. The evolution from this twisted, or sigmoid structure to an arcade is an important mechanism of energy release process as studied in many events (Liu *et al.*, 2005, 2007). (A movie, "mosaic.mpeg", is available on request.)

From the RHESSI light curves, it is evident that the HXR sources were produced during the impulsive phase of the flare, at least in the lower energies of 6 – 12 and 12 – 25 keV. Unfortunately no data were available during 18:17 – 18:36 UT due to the spacecraft night and afterward when the attenuators were out of the field of view. The data with sufficient counts for imaging were available only during 18:00 – 18:10 UT in the impulsive phase of the flare.

We constructed the HXR images with the "CLEAN" algorithm from the modulated data and looked for HXR sources in the flaring region. In Figure 6, we have plotted the contours of these reconstructed images in the energy bands of 3 – 6, 6 – 12 and 12 – 25 keV at 18:09 UT and overlaid on the AIA 171 Å images. The integration time of the images was taken as 1 min, which is adequate to detect the time variations in the HXR sources. Due to the rather low count rates in this event, it was not possible to reconstruct images in higher energy bands.

The HXR contours were found to be localized between the kernels in the flare ribbons, suggesting that the reconnection took place at these HXR source locations, where particles were accelerated along the field lines and propagated toward the foot points anchored in the photosphere. In the 12 – 25 keV image, a break in contours was observed near the center of the eastern ribbon where the emission was weaker. This suggests that the non-thermal HXR sources were located at the foot points on the flare ribbons. In the absence of additional HXR data, however, it was not possible to follow up their further evolution.

3.1.2. The Flare Energetics

We can study the flare energetics by evaluating two main physical parameters, *viz.*, the rates of reconnection and energy release. The reconnection rate which is measured in terms of the electric-field strength in RCS is defined as the reconnected magnetic flux per unit time expressed as

$$\dot{\Phi} = B_{\rm c} v_{\rm in}. \tag{1}$$

The rate of magnetic energy release during a solar flare is the product of the Poynting flux and the area of RCS that is generated during the magnetic reconnection process. On the basis of the reconnection model, it has been shown by Isobe *et al.* (2002) that the energy release rate can be written as

$$\frac{{\rm d}E}{{\rm d}t} = S A_{\rm r} f_{\rm r} = \frac{1}{2\pi} B_{\rm c}^2 v_{\rm in} f_{\rm r}, \tag{2}$$

where S is the Poynting flux into the reconnection region, $B_{\rm c}$, $v_{\rm in}$, $A_{\rm r}$, and $f_{\rm r}$ are coronal magnetic field strength, inflow velocity, area of the reconnection region, and the filling factor of reconnection inflow, respectively.

The inflow velocity can be determined from observations. Using the magnetic flux conservation theorem, one can write

$$B_{\rm c} v_{\rm in} = B_{\rm chrom} v_{\rm ribb} = B_{\rm phot} v_{\rm ribb}, \tag{3}$$

where $v_{\rm ribb}$ is the separation velocity of the Hα ribbons, and $B_{\rm phot}$ and $B_{\rm chrom}$ are the photospheric and chromospheric magnetic field strengths, respectively.

Figure 7 depicts how we measure the separation motion of the flare ribbons along arbitrarily selected lines L1, L2, and L3. We have measured the distances from points marked as "+" on both sides of PIL (thick solid line), *i.e.*, toward the north and south directions. The separation velocities are then determined after fitting the Boltzmann sigmoidal functions through the measurements. Further, using these we calculated the reconnection rates and Poynting fluxes for a quantitative study of flare energetics.

In order to obtain the separation velocity of the flare ribbons, we followed the technique and assumptions as discussed in Maurya and Ambastha (2010) [and references therein] with $a = 0.2$ and $\epsilon = 0.4$. We thus obtained the reconnection rates in the range $0.5 - 3.0$ V cm^{-1} and Poynting fluxes in the range of $0.01 - 3.80 \times 10^9$ erg cm^{-2} s^{-1} as measured along the lines L1, L2, and L3. We have plotted the temporal profiles of them along L2 in Figure 8 in comparison with the rising motion of the filament/CME. This flare lasted for about 3000 s with the current sheet spread over an area $\approx 10^{19}$ cm^2, with an average energy release rate of 10^7 erg cm^{-2} s^{-1}. Using these typical values, we estimate the total energy released during the flare event to be a modest 10^{29} erg, in conformity with the magnitude of the flare. Our results are consistent with that of quiescent filament eruption reported by Wang *et al.* (2003).

We notice here that the motion of the flare kernels was not uniform along the selected lines. Further, the electric field that is expected to release energy through dissipation of

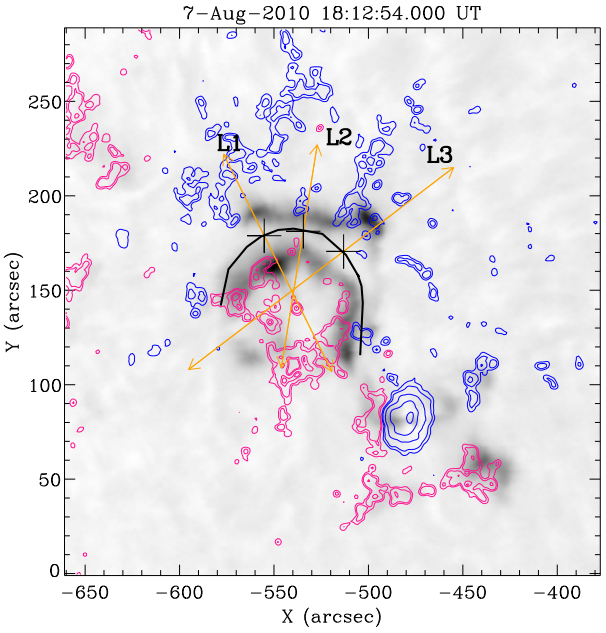

Figure 7 Hα image (in negative) of the flare at 18:12:54 UT, overlaid with magnetic field contours. The solid black line is the simplified PIL. Arrowed lines L1, L2, and L3 are drawn perpendicular to PIL at points marked by "+" to follow the separation of flare ribbons.

electric currents in RCS temporally did not correlate well with the impulsive HXR emission in some directions. To investigate the electron acceleration in the impulsive phase of the flare, we need HXR and microwave observations. However, due to the data gap in HXR observations during the impulsive phase, we have used the time derivative of GOES soft X-ray light curve as a proxy to the HXR intensity with the assumption that the Neupert effect is valid in this event.

Our estimates for this M1.0 flare are lower as compared to the velocities of $15-50\,\mathrm{km\,s^{-1}}$ and reconnection rates of $2.7-11.8\,\mathrm{V\,cm^{-1}}$ for the M3.9 flare reported by Miklenic *et al.* (2007). Also, for a rather short duration and small C9.0 flare, Qiu *et al.* (2002) reported a significantly larger velocity of flare kernels of $20-100\,\mathrm{km\,s^{-1}}$ and peak electric field of $90\,\mathrm{V\,cm^{-1}}$. They found ribbon motions both parallel and perpendicular to PIL and concluded that either the 2D-magnetic reconnection theory related to the Hα kernel motion was applicable only to a part of the flare region due to its particular magnetic geometry, or the electron acceleration was dominated by some other mechanisms depending on the electron energy. We therefore suggest that the estimated electric fields and reconnection rates depend not only on the magnitude of the flare, but also on the flare kernel velocity and the magnetic field geometry.

3.2. The CME and Its Dynamics

The flux rope started rising at 17:40 UT as seen in AIA 304 Å (*cf.* Figure 3). Further, with its rise, the surrounding overlying loops also started rising as if they formed a balloon-like cavity expanding temporally. The jet-like ejection of plasma came out from the reconnection region with ejection velocity presumably proportional to the reconnection rate as its height increased. Eventually, it was observed as a CME event in the COR1 coronagraph at about 18:20 UT.

We have made the projection of the lateral displacements of the filament into the vertical direction using the AIA 304 Å images in the pre-rise phase (see Wang *et al.* (2003)

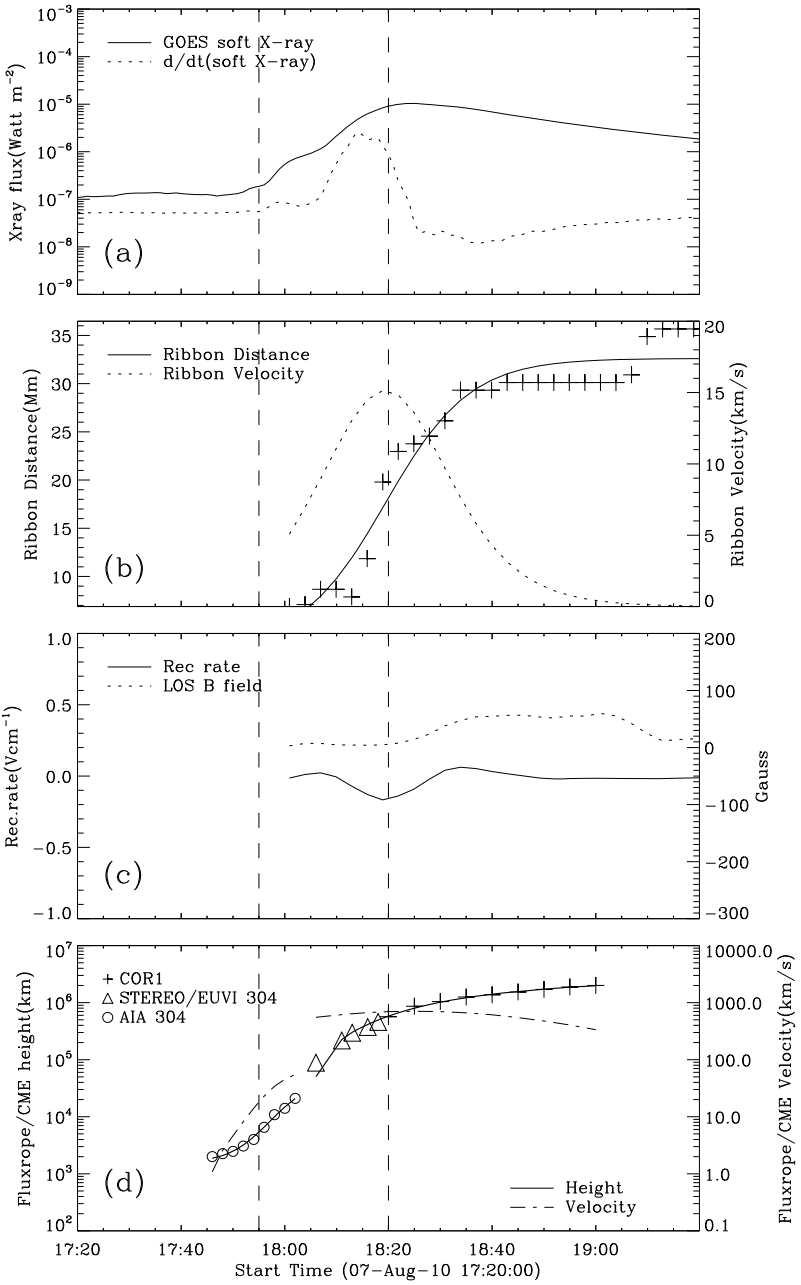

Figure 8 (a) GOES X-ray flux and its time derivative, (b) separation distance and velocity of the flare ribbons, (c) reconnection rate and Poynting flux, and (d) filament/flux rope height as a function of time. Vertical dashed lines mark the start and peak times of the flare for reference.

for details), and corrected for the heights of the flux rope as if it was seen exactly on the limb in STEREO/EUVI in the impulsive phase. Then we reconstructed the heights of the CME front end from the triangulation method in the decay phase to obtain the heights of filament/flux rope with its rise. In order to reduce the measurement errors, we fit them with the Boltzmann sigmoidal function as used for the analysis of the motion of the flare ribbons (Maurya and Ambastha, 2010). This function suits well as a model to the data because the lower (steep) and upper parts of this function resemble the rise, impulsive, and decay phases of the CME/flux rope dynamics and can be fitted by four parameters in the least square sense.

The heights of the filament and the CME front thus derived are plotted in Figure 8 in comparing with the temporal evolution of the flare ribbon separation, filament eruption, and flare energy release in terms of the reconnection rate (Wang *et al.*, 2003). The fast-rising stage coincided with the flare impulsive phase, and the mass acceleration increased rapidly along with the increase of the magnetic reconnection rate. As evident from the figure, the flare ribbons appeared at 17:58 UT and attained their maximum velocity at the peak phase of the flare. This motion agreed with the HXR profile as electrons injected onto the photosphere in the impulsive phase with increasing reconnection rate. From the figure, we can see that the filament started to rise in the first 15 minutes with velocities in the range of $8-10$ km s^{-1}, reaching 100 km s^{-1} at an average acceleration of 60 m s^{-2}. From the STEREO observations including COR1, we found that the CME traveled with an average speed of 590 km s^{-1} and reached its peak acceleration of 220 m s^{-2} at the peak phase of the flare. It then decelerated in the decay phase gradually. The correlation between the magnetic reconnection rate and the acceleration of flux ropes was found in a study of 13 well observed two-ribbon flares by Jing *et al.* (2005). Our results are also consistent with theirs of accelerations in the range of $50-400$ m s^{-2} up to 3 km s^{-2} with peak reconnection rates in the range of $0.2-5.0$ V cm^{-1}.

3.3. Changes in the Photospheric Magnetic Field

Theoretical models suggest that the evolution of magnetic fields at or below the photosphere, in the form of flux emergence and cancelation, could result in a loss of equilibrium of magnetic structures (Martin, Livi, and Wang, 1985; Martin, 1989; Leka *et al.*, 1996). Changes in the photospheric longitudinal magnetic field around the time of the eruption have been examined by many workers in the past (Wang and Sheeley, 1999; Mathew and Ambastha, 2000; Green *et al.*, 2003; Ambastha, 2007; Jiang, Shen, and Wang, 2007; Sterling, Harra, and Moore, 2007). Zhang, Zhang, and Zhang (2008) studied the relationship between the flux emergence and CME initiation inferring that 60% of CME source regions showed increase and 40% have showed decrease in magnetic flux.

Here, we look for regions, if any, of flux emergence/cancelation in the photospheric LOS magnetic field using high resolution SDO/HMI magnetograms. We carried out registration of the images by differentially rotating them to a reference image at 18:00 UT. Effects of telescope jitter and other pointing errors were corrected by using a cross correlation method reducing the uncertainty within $1-2$ arcsec. Every four images were added to yield a cadence of 3 minutes. As the sensitivity of HMI is around 10 G, we neglected magnetic fields below this value.

A typical GONG Hα image of NOAA 11093 overlaid with contours of LOS magnetic fields is shown in Figure 9 (left panel). From a movie of the registered images, we identified several sites of flux emergence/cancelation, marked in the figure by boxes, located around the filament and the sunspot in the AR. The time profiles of unsigned magnetic fluxes corresponding to the selected boxes are plotted during the period of 16:00 – 20:00 UT. Sufficient

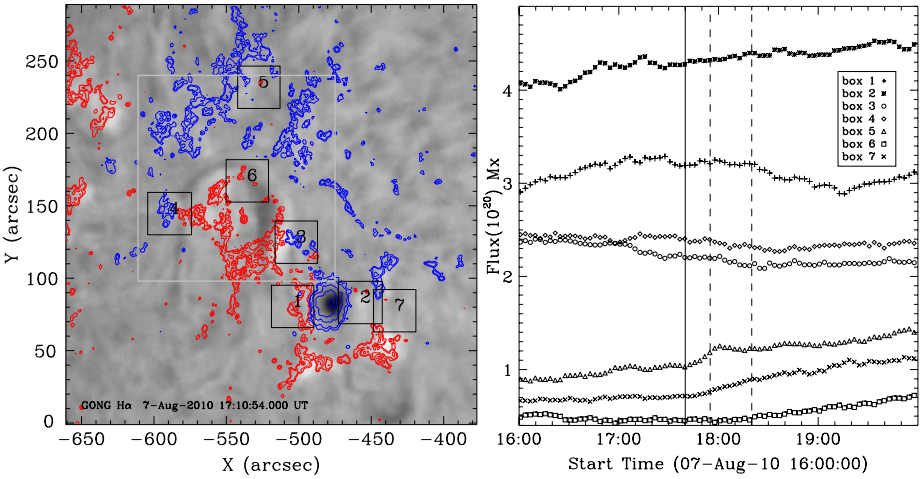

Figure 9 (Left) GONG Hα image of NOAA11093 overlaid with HMI LOS magnetogram contours. Boxes (1 – 7) mark the selected regions-of-interest (ROI) for the calculation of unsigned flux. (Right): Temporal profiles of unsigned flux in the ROIs.

care was taken in selecting the box size of $30'' \times 30''$. A very small box size would not adequately cover the region of interest, while averaging over too large a region would dilute the magnitude of changes.

In the following we present the temporal evolution of magnetic flux in each box and its contribution to the stability of sunspot-filament magnetic system. Boxes 1 and 2 are located around the leading sunspot. Box 1 was selected at the penumbra of the sunspot and covered the regions of opposite polarity fluxes around the filament. The total unsigned flux increased there till the time of onset of the filament eruption, and decreased thereafter. On the other hand, changes were oscillatory in box 2 before the flare, where a small region of negative (red) flux emerged along with the pre-flare brightening.

Boxes 3, 4, 5, and 6 are located at either side of the PIL from where field lines originated to tie the filament down as required for a stable configuration. Changes in these boxes are important for examining the stability of the filament. In box 3, a gradual decrease in magnetic flux of 0.2×10^{20} Mx (maxwell) occurred at the flare onset time (the time of start of the rope rise). On the other hand, the flux increased in boxes 5, 6, and 7 as a result of new flux emergence. Of these, box 6 was located under the flux rope. Evidently, there were sites of flux emergence/cancelation in and around the filament influencing its stability. As the HMI measurements do not suffer from the degrading effect of Earth's atmosphere, one can be reasonably confident about the observed flux changes.

To further corroborate these temporal changes, we enlarged some ROIs as shown in Figure 10 (top panel). Several emerging flux regions (EFR), marked by arrows, can be seen in these regions. However, we did not find appreciable disappearance or cancelation in box 3. We also looked for any brightening expected to be associated with flux emergence/cancelation, by examining difference images of the pre-eruption/flare phase, *i.e.*, 17:45 – 17:40 UT, in AIA 171 Å and 304 Å images (Figure 10, bottom panel). This showed a brightening (seen as darkening in the difference images) in box 3 where a gradual decrease of unsigned flux was observed during the rise phase of the filament. Similar changes were also found in boxes 5 and 7 (seen as white dots in the difference images).

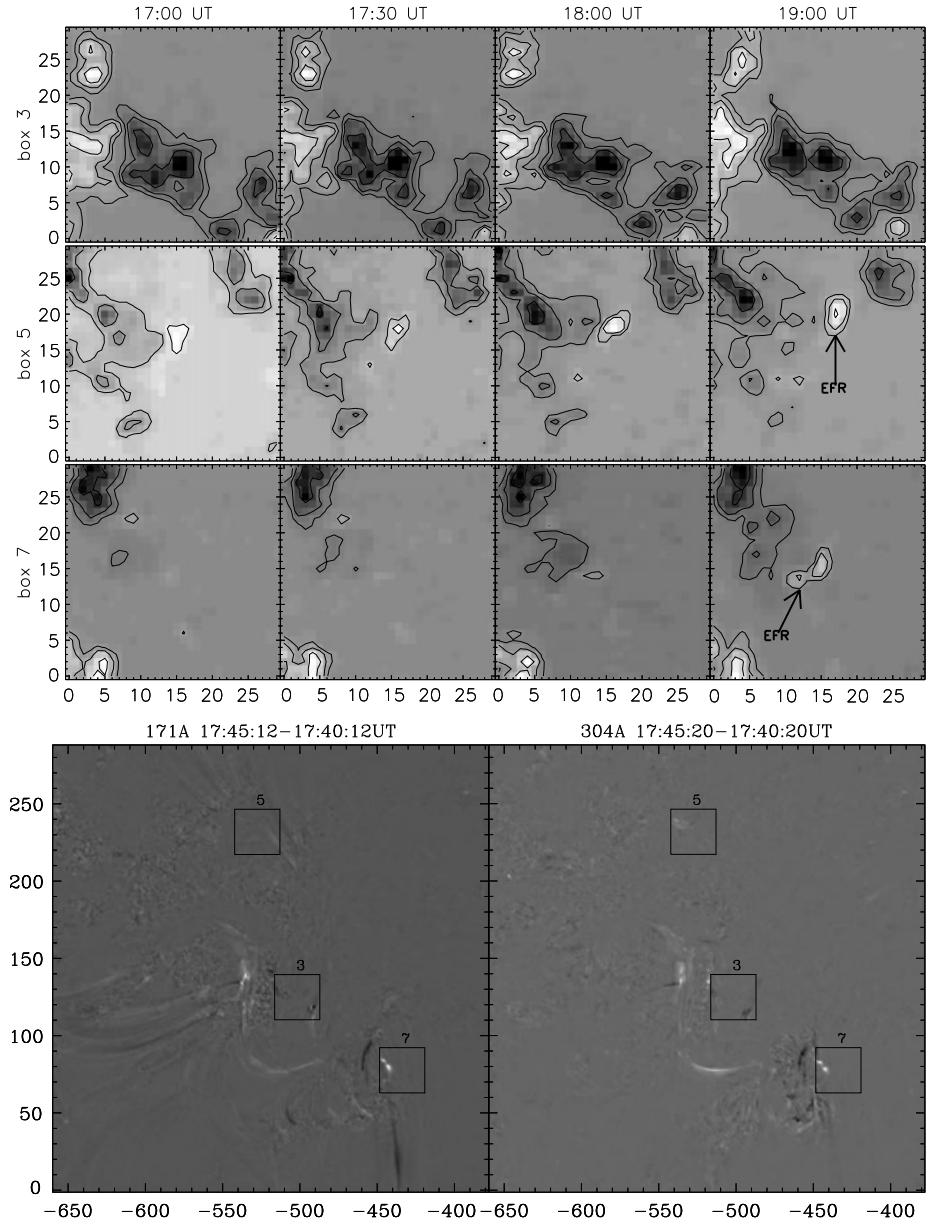

Figure 10 Enlarged box regions 3, 5 and 7 of Figure 9, showing the evolution of magnetic flux with time (top panel). Difference images in the pre-eruption/flare phase of 17:45 – 17:40 UT in AIA 171 Å and 304 Å wavelengths showing associated brightenings (bottom panel).

In a recent work, Wang and Liu (2010) found observational evidence of back reaction on the solar surface magnetic fields from the restructuring of coronal magnetic fields after reconnection in well observed X-class flares. This restructuring can be seen as increased limb-ward flux with the corresponding decreased disk-ward flux due to projection effects in

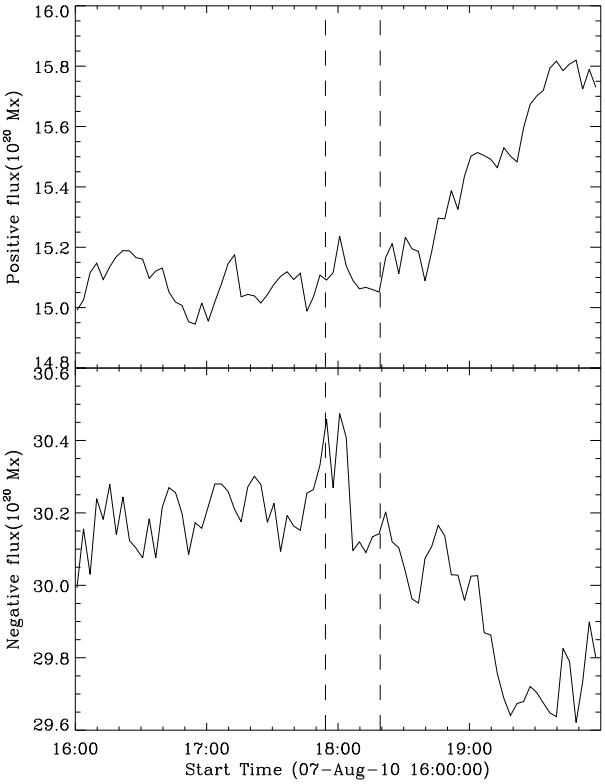

Figure 11 Time profiles of positive and negative fluxes within the region covering the entire filament area (gray big box in Figure 9 (left panel)). The start and peak times of the flare are marked by the dashed vertical lines.

LOS fields. They suggested that such results may also be detectable for smaller flares from higher-sensitivity HMI data. To investigate it, we computed positive and negative fluxes separately in the region shown as the large box (drawn in gray color in Figure 9 (left panel)) covering the filament. Figure 11 shows that positive/negative (limbward/diskward) fluxes increased/decreased by a similar amount of $\approx 10^{20}$ Mx in the post-flare phase. This gives an indirect evidence of reconnection as a consequence of tether cutting, mentioned in the previous sections.

Thus, we have found regions of flux emergence, cancelation and associated EUV brightening in some locations of the AR (see Figure 3(a)). The interaction of field lines at one of these brightening regions gives evidence of reconnection leading to tether weakening. These processes could have destabilized the filament to rise upward leading to the tether-cutting reconnection. The photospheric flux changes found in the decay phase of the event are in conformity with Wang and Liu (2010), *i.e.*, evidence of the back reaction on the surface magnetic fields as a consequence of reconnection.

4. Summary and Conclusions

The current models assume that the stored energy lies in a low lying magnetic flux system which is twisted or sheared. This system is the so-called core flux or flux rope. Such twisted systems in the form of forward or inverse S, called sigmoids, are usually seen in association with eruptions as the present event. Canfield, Hudson, and McKenzie (1999) had studied

the nature of activity with respect to the morphology of eruptive or non-eruptive events with soft X-ray observations and inferred that sigmoids are more likely to erupt.

In this paper, we have presented multi-instrument multi-wavelength observations and analysis of the eruption of an inverse S-shaped filament. This event exhibits a good example of the standard solar flare characterized by the filament eruption, two-ribbon separation, and its association with a fast CME. We now summarize the main findings of our analysis of this eruption event:

1. From a morphological study of this event, we inferred that the rising motion of the filament was triggered by remote tether weakening at a coronal brightening region, which further induced the tether-cutting reconnection underneath it to unleash the eruption process, leading to a fast CME subsequent to the two-ribbon flare.
2. Flare ribbons or kernels separated out with modest velocities in the range of 12 – 16 km s^{-1}. This was used to estimate various physical parameters for evaluating the flare energetics using a 2-D model. Reconnection rates and Poynting fluxes were estimated in the range of 0.5 – 3.0 V cm^{-1} and 0.01 – 3.8 $\times 10^9$ erg cm^{-2} s^{-1}, respectively. These were sufficient to release a free energy of 10^{29} erg of an M-class flare.
3. The rising motion of the filament/flux rope indeed showed correspondence with various flare characteristics, *viz.*, reconnection rate and hard X-ray emission profiles. It started rising with a velocity of 8 – 10 km s^{-1}, reaching a maximum of around 100 km s^{-1} with an average acceleration of 60 m s^{-2} (estimated by projecting the lateral displacements of the filament on to the vertical direction observed in the 304 Å channel of AIA). Further, this flux rope was accelerated to the maximum velocity as a CME, observed at the peak phase of the flare, followed by its deceleration to an average velocity of 590 km s^{-1}.
4. Magnetic flux variations in and around the filament were examined before and after the eruption. We found some areas of flux changes, co-temporal with the onset of the filament rise. For example, gradual reduction of positive flux was found in box 3 (*cf.* Figure 9) at the onset time of the filament rise. From a careful study of 171 Å images, it is interpreted as a consequence of the interaction between the overlying field lines across the filament and the side-lobe field lines, resulting in tether weakening of the sigmoidal filament system. In addition, flux emergence in box 5 located near the rising part of the filament might have contributed to the destabilization of the system. In summary, we infer that these flux changes caused the loss of equilibrium leading to a slow, upward rise of the filament, and the onset of eruption by the tether-cutting reconnection. In turn, changes occurred in photospheric magnetic fluxes in the decay phase of the flare as a back reaction of this reconnection (Figure 11), in accordance with the recent findings of Wang and Liu (2010).

Destabilization of the filament system can occur due to either ideal-MHD, or kink, instability (Kliem and Török, 2006). An increased twist in the filament or flux rope system may result from flux emergence, because of which the filament itself can rise. Another possibility could be shear motions of photospheric fluxes, which were not studied here. We suggest that the observed emergence/cancelation of magnetic fluxes near the filament caused the flux rope to rise, resulting in the tethers to cut and reconnection to take place beneath the filament; in agreement with the tether-cutting model. We intend to pursue this study further by invoking observations of vector magnetograms as boundary conditions for extrapolations to look for changes in the coronal magnetic field and other associated parameters.

Acknowledgements The AIA (HMI) data used here are courtesy of SDO (NASA) and the AIA (HMI) consortium. We thank the AIA team for making available the processed data. This work utilizes data obtained by the Global Oscillation Network Group (GONG) Program, managed by the National Solar Observatory,

which is operated by AURA, Inc., under a cooperative agreement with the National Science Foundation. We thank the anonymous referees for carefully going through the manuscript and making valuable comments which improved the readability of the manuscript appreciably.

References

Ambastha, A.: 2007, *Sun Geosph.* **2**, 13.
Antiochos, S.K.: 1998, *Astrophys. J. Lett.* **502**, L181.
Antiochos, S.K., DeVore, C.R., Klimchuk, J.A.: 1999, *Astrophys. J.* **510**, 485.
Canfield, R.C., Hudson, H.S., McKenzie, D.E.: 1999, *Geophys. Res. Lett.* **26**, 627.
Carmichael, H.: 1964, In: Hess, W.N. (ed.) *Physics of Solar Flares, NASA SP-50*, 451.
Fan, Y., Gibson, S.E.: 2007, *Astrophys. J.* **668**, 1232.
Forbes, T.G.: 2006, *Space Sci. Rev.* **123**, 251.
Forbes, T.G., Priest, E.R.: 1984, *Solar Phys.* **94**, 315.
Green, L.M., Démoulin, P., Mandrini, C.H., Van Driel-Gesztelyi, L.: 2003, *Solar Phys.* **215**, 307.
Hirayama, T.: 1974, *Solar Phys.* **34**, 323.
Isobe, H., Yokoyama, T., Shimojo, M., Morimoto, T., Kozu, H., Eto, S., Narukage, N., Shibata, K.: 2002, *Astrophys. J.* **566**, 528.
Jiang, Y., Shen, Y., Wang, J.: 2007, *Chin. J. Astron. Astrophys.* **7**, 129.
Jing, J., Qiu, J., Lin, J., Qu, M., Xu, Y., Wang, H.: 2005, *Astrophys. J.* **620**, 1085.
Kliem, B., Török, T.: 2006, *Phys. Rev. Lett.* **96**, 255002.
Klimchuk, J.A.: 2001, In: Song, P., Singer, H., Siscoe, G. (eds.) *Space Weather*, *AGU Geophys. Monogr.* **125**, 143.
Kopp, R.A., Pneuman, G.W.: 1976, *Solar Phys.* **50**, 85.
Leka, K.D., Canfield, R.C., McClymont, A.N., van Driel-Gesztelyi, L.: 1996, *Astrophys. J.* **462**, 547.
Lemen, J.R., Title,A.M., Akin, D.J., Boerner, P.F., Chou, C., Drake, J.F., *et al.*: 2011, *Solar Phys.* doi:10.1086/177171.
Lin, J., Forbes, T.G.: 2000, *J. Geophys. Res.* **105**, 2375.
Lin, J., Soon, W., Baliunas, S.L.: 2003, *New Astron. Rev.* **47**, 53.
Lin, R.P., Dennis, B.R., Hurdford, G.J., Smith, D.M., Zehnder, A., Harvey, P.R., *et al.*: 2002, *Solar Phys.* **210**, 3.
Litvinenko, Y.E., Somov, B.V.: 1995, *Solar Phys.* **158**, 317.
Liu, C., Lee, J., Yurchyshyn, V., Deng, N., Cho, K., Karlický, M., Wang, H.: 2007, *Astrophys. J.* **669**, 1372.
Liu, Y., Su, J.T., Morimoto, T., Kurokawa, H., Shibata, K.: 2005, *Astrophys. J.* **628**, 1056.
Martens, P.C.H., Young, A.: 1990, *Astrophys. J. Suppl.* **73**, 333.
Martin, S.F.: 1989, *Solar Phys.* **121**, 215.
Martin, S.F., Livi, S.H.B., Wang, J.: 1985, *Aust. J. Phys.* **38**, 929.
Mathew, S.K., Ambastha, A.: 2000, *Solar Phys.* **197**, 75.
Maurya, R.A., Ambastha, A.: 2010, *Solar Phys.* **262**, 337.
Miklenic, C.H., Veronig, A.M., Vršnak, B., Hanslmeier, A.: 2007, *Astron. Astrophys.* **461**, 697.
Moore, R.L., LaBonte, B.J.: 1980, In: Dryer, M., Tandberg-Hanssen, E. (eds.) *Solar and Interplanetary Dynamics*, *IAU Symp.* **91**, 207.
Moore, R.L., Sterling, A.C.: 2006, In: Gopalswamy, N., Mewaldt, R., Torsti, J. (eds.) *Solar Eruptions and Energetic Particles*, *AGU Geophys. Monogr.* **165**, 43.
Moore, R.L., Sterling, A.C., Hudson, H.S., Lemen, J.R.: 2001, *Astrophys. J.* **552**, 833.
Priest, E.R., Forbes, T.G.: 2002, *Astron. Astrophys. Rev.* **10**, 313.
Qiu, J., Lee, J., Gary, D.E., Wang, H.: 2002, *Astrophys. J.* **565**, 1335.
Schou, W., Scherrer, P.H., Bush, R.I., Wachter, R., Couvidat, S., Rabello-Soares, M.C., *et al.*: 2011, *Solar Phys.* doi:10.1007/s11207-011-9842-2.
Sterling, A.C., Harra, L.K., Moore, R.L.: 2007, *Astrophys. J.* **669**, 1359.
Sturrock, P.A.: 1966, *Nature* **211**, 695.
Thompson, W.T., Davila, J.M., Fisher, R.R., Orwig, L.E., Mentzell, J.E., Hetherington, S.E.: 2003, In: Keil, S.L., Avakyan, S.V. (eds.) *Innovative Telescopes and Instrumentation for Solar Astrophysics*, *Proc. SPIE* **4853**, 1.
Wang, H.: 2006, *Astrophys. J.* **649**, 490.
Wang, H., Liu, C.: 2010, *Astrophys. J. Lett.* **716**, L195.
Wang, H., Qiu, J., Jing, J., Zhang, H.: 2003, *Astrophys. J.* **593**, 564.
Wang, Y., Sheeley, N.R. Jr.: 1999, *Astrophys. J. Lett.* **510**, L157.
Yurchyshyn, V., Karlický, M., Hu, Q., Wang, H.: 2006, *Solar Phys.* **235**, 147.
Zhang, Y., Zhang, M., Zhang, H.: 2008, *Solar Phys.* **250**, 75.